The Astrophysical Journal Letters, 959:L26 (13pp), 2023 December 20 https://doi.org/10.3847/2041-8213/ad0e6b


# Early-time Ultraviolet and Optical Hubble Space Telescope Spectroscopy of the Type II Supernova 2022wsp

Sergiy S. Vasylyev[1,2], Christian Vogl[3], Yi Yang (杨轶)[1,4], Alexei V. Filippenko[1], Thomas G. Brink[1,5], Peter J. Brown[6], Thomas Matheson[7], Maryam Modjaz[8], Avishay Gal-Yam[9], Paolo A. Mazzali[3], Thomas de Jaeger[10], Kishore C. Patra[1,11], and Gabrielle E. Stewart[1]
[1] Department of Astronomy, University of California, Berkeley, CA 94720-3411, USA; sergiy_vasylyev@berkeley.edu, yiyangtamu@gmail.com
[2] Steven Nelson Graduate Fellow in Astronomy
[3] Max-Planck-Institut für Astrophysik, Karl-Schwarzschild-Str. 1, D-85748 Garching, Germany
[4] Bengier-Winslow-Robertson Postdoctoral Fellow in Astronomy
[5] Wood Specialist in Astronomy
[6] George P. and Cynthia Woods Mitchell Institute for Fundamental Physics and Astronomy, and Department of Physics and Astronomy, Texas A&M University, 4242 TAMU, College Station, TX 78712, USA
[7] NSF's National Optical-Infrared Astronomy Research Laboratory, 950 North Cherry Avenue, Tucson, AZ 85719, USA
[8] Department of Astronomy, University of Virginia, Charlottesville, VA 22903, USA
[9] Department of Particle Physics and Astrophysics, Weizmann Institute of Science, 234 Herzl St., 76100 Rehovot, Israel
[10] LPNHE, CNRS/IN2P3 & Sorbonne Université, 4 place Jussieu, F-75005 Paris, France
[11] Nagaraj-Noll-Otellini Graduate Fellow in Astronomy
*Received 2023 April 12; revised 2023 October 28; accepted 2023 October 31; published 2023 December 20*

## Abstract

We report early-time ultraviolet (UV) and optical spectroscopy of the young, nearby Type II supernova (SN) 2022wsp obtained by the Hubble Space Telescope (HST)/STIS at about 10 and 20 days after the explosion. The SN 2022wsp UV spectra are compared to those of other well-observed Type II/IIP SNe, including the recently studied Type IIP SN 2021yja. Both SNe exhibit rapid cooling and similar evolution during early phases, indicating a common behavior among SNe II. Radiative-transfer modeling of the spectra of SN 2022wsp with the TARDIS code indicates a steep radial density profile in the outer layer of the ejecta, a solar metallicity, and a relatively high total extinction of $E(B-V)=0.35$ mag. The early-time evolution of the photospheric velocity and temperature derived from the modeling agree with the behavior observed from other previously studied cases. The strong suppression of hydrogen Balmer lines in the spectra suggests interaction with a preexisting circumstellar environment could be occurring at early times. In the SN 2022wsp spectra, the absorption component of the Mg II P Cygni profile displays a double-trough feature on day +10 that disappears by day +20. The shape is well reproduced by the model without fine-tuning the parameters, suggesting that the secondary blueward dip is a metal transition that originates in the SN ejecta.

*Unified Astronomy Thesaurus concepts:* Ultraviolet spectroscopy (2284); Spectroscopy (1558)

*Supporting material:* data behind figure

## 1. Introduction

Type II supernovae (SNe) are characterized by the detection of hydrogen in their optical spectra. They can be differentiated photometrically by the shape of their light curve, which is primarily determined by the thickness of the hydrogen envelope of the exploding progenitor star.

An SN II with a light curve that declines linearly in magnitude is classified as an SN IIL, while an SN II with a plateau lasting ~100 days after the explosion is categorized as an SN IIP. Interaction is also suggested to be important for the linear decline seen in SNe IIL. However, recent studies suggest that the light curves of Type II SNe exhibit a continuous range of declines, indicating that the distinction between the SN IIP and SN IIL is not clear cut (Anderson et al. 2014; Sanders et al. 2015; Rubin & Gal-Yam 2016; Valenti et al. 2016). The explosion mechanism producing Type II and a subset of Type I (Ib/Ic; stripped-envelope) SNe is widely accepted to be the core collapse of a star with zero-age main-sequence (ZAMS) mass $\geqslant 8\ M_{\odot}$; see Filippenko (1997), Gal-Yam (2017), and Modjaz et al. (2019) for reviews. However, the precise mechanism by which these explosions occur is not clear.

The spectral continuum of an SN II peaks in the ultraviolet (UV) in the days and weeks following the explosion, and then continues to shift toward optical wavelengths over the next few months through a combination of cooling and line blanketing. Distinguishing the SN type at early times is challenging, as SN II spectra often resemble those of SNe Ic (see, for example, Williamson et al. 2023). Although the optical spectra of core-collapse SNe (CCSNe) have been extensively studied, the sample of UV spectra of CCSNe still remains scarce. This is in part due to the challenging nature of these observations, as they require rapid follow-up spectroscopy from space-based telescopes within three weeks after the SN explosion, before the radiation peak shifts from the UV to longer wavelengths. Moreover, the SNe must be sufficiently nearby to achieve a decent signal-to-noise ratio (S/N) in the UV. Additionally, some SNe may have their UV flux suppressed by dust attenuation along the line of sight. Despite these challenges, several programs have made significant strides in obtaining and analyzing UV spectra of SNe II. UV spectroscopy has been carried out for only a handful of SNe IIP, demonstrating a relatively high degree of uniformity in their

UV (2000–3500 Å) spectroscopic properties at ∼10 days after the explosion (Gal-Yam et al. 2008; Bufano et al. 2009; Bayless et al. 2013; Dhungana et al. 2016). Building on this research, Vasylyev et al. (2022) expanded the sample by including SN 2021yja and demonstrating its resemblance to these H-rich CCSNe.

The UV spectra of SNe IIP are also observed to have shared spectral line features. For example, SN IIP UV spectra show the characteristic Mg II $\lambda$2798 P Cygni profile and several relatively broad emission "bumps" around 2200, 2400, and 2600 Å. These features can be attributed to a series of blended Fe II and Ni II lines (Brown et al. 2007; Gal-Yam et al. 2008; Bufano et al. 2009; Dhungana et al. 2016). The sample size utilized in this study is limited and predominantly derived from a subset of SNe II that have been observed through Hubble Space Telescope (HST) and Swift/UVOT programs. In order to gain a more comprehensive understanding of the properties and behavior of their UV spectra, it is essential to obtain a larger sample that allows further exploration of any commonality and diversity among SNe II. Nevertheless, the results from these studies provide a crucial baseline to develop a comprehensive understanding of the nature of these commonly seen H-rich CCSNe.

Early-time UV spectra provide critical information about the dynamics and composition of the exploding star since they are highly sensitive to the velocity of the expanding ejecta and the temperature. Additionally, the line species and their strengths reflect the metallicity and surface composition of the exploding star, thus tracing the preexplosion behavior (Mazzali 2000; Dessart & Hillier 2005, 2006). Moreover, the UV flux is an excellent probe of the circumstellar environment of the progenitor, allowing one to identify additional heating sources such as interaction with the circumstellar medium (CSM; Ben-Ami et al. 2015).

Here we present two early-time UV spectra of a relatively nearby, young, and moderately reddened Type IIP SN 2022wsp (DLT22q). The event was discovered on 2022 October 2 at 23:59:19 (UTC dates are used throughout this paper) in the spiral galaxy NGC 7448 by the Distance Less Than 40 (DLT40; Tartaglia et al. 2018) survey (see Bostroem et al. 2022). The SN was first detected at 17.1 mag with the clear filter. The last nondetection was on October 2. 03:51:46, with an upper limit of 19.6 mag through a clear filter. Follow-up ground-based spectroscopy conducted on October 5 23:46 suggested that SN 2022wsp was an SN II a few days after the explosion (Nagao et al. 2022). A "preferred" redshift of $z = 0.00732$ was reported by Lu et al. (1993), and a distance of $25.04 \pm 1.79$ Mpc can be queried from the NASA/IPAC NED Database based on the cosmic microwave background redshift and the assumption of a Hubble constant of $H_0 = 73$ km s$^{-1}$ Mpc$^{-1}$ (Riess et al. 2022).

We requested target of opportunity observations with HST to obtain UV and optical spectra of SN 2022wsp (GO-16656; PI A. Filippenko). This Letter, which presents the UV and optical spectroscopy at relatively early phases, is organized as follows. Section 2 summarizes the HST observations. In Section 3 we analyze the data based on TARDIS (a one-dimensional Monte Carlo radiative-transfer code) fitting of the spectra. A summary of the study is given in Section 4.

## 2. Observations

### 2.1. HST/STIS

The explosion date of SN 2022wsp was estimated as the midpoint between the last nondetection (MJD 59854.16) and the first detection (MJD 59855.00) by the DLT40 survey, which gives MJD $59854.58 \pm 0.42$ (Bostroem et al. 2022). HST UV and optical follow-up spectroscopy of SN 2022wsp was executed on 2022 October 12 and 22, corresponding to +10 and +20 days after the explosion, respectively. Owing to technical and scheduling issues, the third epoch of observations was delayed until more than three months after the explosion. Unfortunately, by this time, the UV radiation of the SN had faded below the threshold required for proper spectral analysis; the peak of the SN spectral energy distribution had moved to optical wavelengths. The third epoch of our HST optical observations of SN 2022wsp will be presented in future work, together with a comprehensive analysis of the photometric, spectroscopic, and polarimetric properties of the SN until the nebular phase (Vasylyev et al., 2023, in preparation).

All spectroscopy was carried out using the CCD ($52'' \times 52''$ field of view) and the Near-UV Multi-Anode MicroChannel Array (NUV-MAMA) detectors of the Space Telescope Imaging Spectrograph (STIS; Prichard et al. 2022). For Epochs 1 and 2, observations of the mid-UV (15703180 Å) with the G230L grating were made across six orbits of integration. One visit per epoch was used for the near-UV (2900–5700 Å) and optical (5240–10270 Å) ranges with the G430L and G750L gratings, respectively. A detailed log of the HST observations can be found in Table 1. The UV-optical spectra at +10 and +20 days are presented in Figure 1. All the HST data used in this paper can be found at MAST doi:10.17909/0dxs-xd86.

## 3. Analysis and Discussion

In this section, we examine the spectra of SN 2022wsp through a comparison with those of other well-sampled Type II and Type IIP SNe. This includes a discussion of the dust properties along the line of sight to the explosion and the modeling of the UV-optical spectra with TARDIS.

### 3.1. Dust Extinction

The Galactic reddening along the line of sight to SN 2022wsp gives $E(B-V)_{\rm MW} = 0.05$ mag, according to the extinction map derived by Schlafly & Finkbeiner (2011). We determined that the host galaxy also contributes significantly to the extinction ($E(B-V)_{\rm host} = 0.3$ mag), which results in a combined reddening value of $E(B-V)_{\rm tot} = 0.35$ mag (see Section 3.4). The relatively high reddening value of the SN is consistent with the explosion site being projected close to the nucleus of the host galaxy. The SN 2022wsp spectra presented in this work are dereddened by the total extinction adopting an $R_{\rm V} = 3.1$ dust law and the CCM89 model (Cardelli et al. 1989) unless otherwise specified. All of the spectra have been corrected for the recession of the host galaxy NGC 7448 using $z = 0.00732$ (NED/IPAC Extragalactic Database23;[12] Lu et al. 1993).

### 3.2. The Early-time UV Spectrum

Here, we examine the UV spectral properties of SN 2022wsp and compare them with those of SN 2021yja as presented by Vasylyev et al. (2022) and with other SNe IIP having high-S/N UV data.

In Figure 1, we present the HST/STIS UV-optical spectra of SN 2022wsp obtained on days +10 and +20. For comparison,

[12] See https://ned.ipac.caltech.edu/.

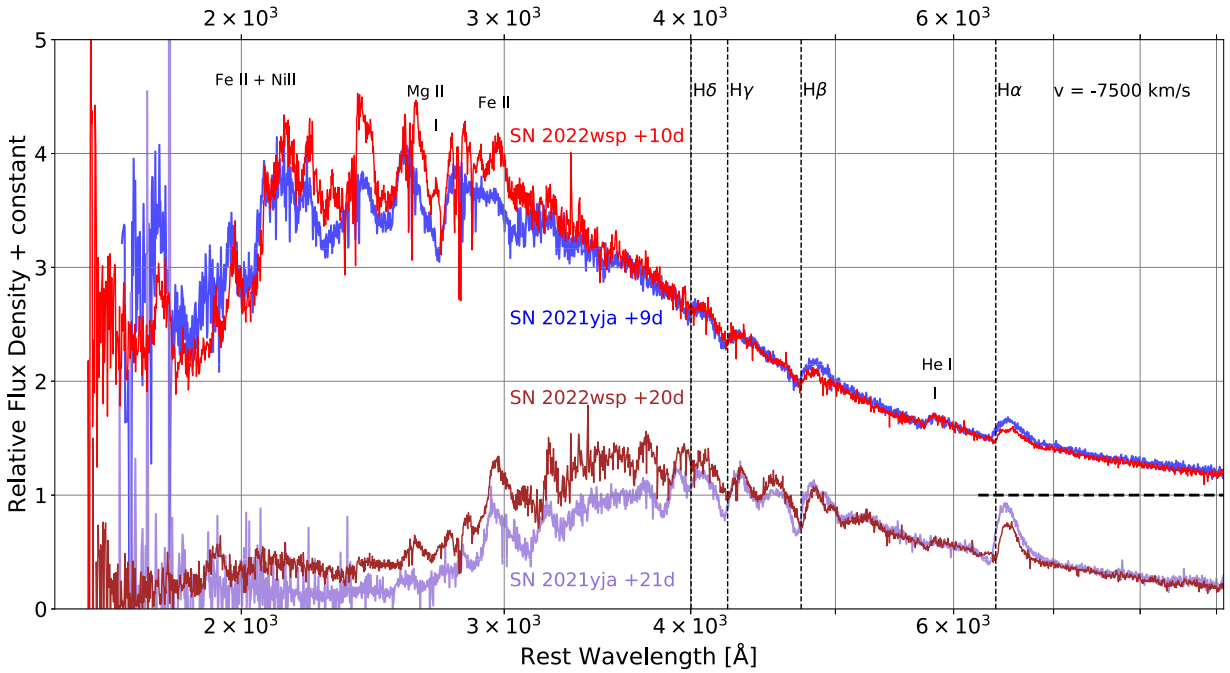


**Figure 1.** HST/STIS UV-optical spectra of SN 2022wsp at +10 and +20 days compared with those of SN 2021yja at similar phases. All spectra have been dereddened. The SN 2022wsp flux density has been scaled by the same constant for both days such that the continuum level redward of 7000 Å matches that of SN 2021yja, demonstrating the dramatic evolution and variation in the UV, while showing general agreement at optical wavelengths. The spectra have also been shifted arbitrarily by a constant for easier comparison. The wavelength scale has been corrected to the rest frame using the recession velocity of the host galaxy. Balmer lines at an expansion velocity of $v = 7500$ km s$^{-1}$ are marked by vertical dotted lines. The zero flux level of the top two spectra is indicated by the horizontal dashed line.

(The data used to create this figure are available.)

**Table 1**
HST Observation Log for SN 2022wsp (GO-16656; PI A. Filippenko)

| Start Time (UTC) | Stop Time (UTC) | Exp. (s) | Grating/Filter | $\lambda_0$ (Å) |
|---|---|---|---|---|
| 2022-10-12 10:30:55 | 2022-10-12 11:09:01 | 2286 | G230L | 2376 |
| 2022-10-12 11:57:50 | 2022-10-12 12:43:26 | 2736 | G230L | 2376 |
| 2022-10-12 13:33:03 | 2022-10-12 14:18:39 | 2736 | G230L | 2376 |
| 2022-10-12 15:20:08 | 2022-10-12 15:53:53 | 2025 | G230L | 2376 |
| 2022-10-12 16:43:31 | 2022-10-12 17:29:07 | 2736 | G230L | 2376 |
| 2022-10-12 18:18:46 | 2022-10-12 18:34:39 | 953 | G230L | 2376 |
| 2022-10-12 18:38:15 | 2022-10-12 18:52:19 | 800 | G430L | 4300 |
| 2022-10-12 18:56:28 | 2022-10-12 19:03:52 | 400 | G750L | 7751 |
| 2022-10-22 07:03:54 | 2022-10-22 07:42:00 | 2286 | G230L | 2376 |
| 2022-10-22 08:30:50 | 2022-10-22 09:16:26 | 2736 | G230L | 2376 |
| 2022-10-22 10:06:06 | 2022-10-22 10:51:42 | 2736 | G230L | 2376 |
| 2022-10-22 11:53:12 | 2022-10-22 12:26:57 | 2025 | G230L | 2376 |
| 2022-10-22 13:16:35 | 2022-10-22 14:02:11 | 2736 | G230L | 2376 |
| 2022-10-22 14:51:51 | 2022-10-22 15:07:44 | 953 | G230L | 2376 |
| 2022-10-22 15:11:20 | 2022-10-22 15:25:24 | 800 | G430L | 4300 |
| 2022-10-22 15:29:33 | 2022-10-22 15:36:57 | 400 | G750L | 7551 |
| 2023-01-10 13:23:24 | 2023-01-10 14:01:30 | 2286 | G230L | 2376 |
| 2023-01-10 14:50:14 | 2023-01-10 15:35:50 | 2736 | G230L | 2376 |
| 2023-01-10 16:25:25 | 2023-01-10 17:11:01 | 2736 | G230L | 2376 |
| 2023-01-10 18:12:28 | 2023-01-10 18:46:13 | 2025 | G230L | 2376 |
| 2023-01-10 19:35:40 | 2023-01-10 20:02:49 | 1585 | G430L | 4300 |
| 2023-01-10 20:06:58 | 2023-01-10 20:20:54 | 792 | G750L | 7551 |

we also display the spectra of SN 2021yja obtained on days +9 and +21. Identifications of the major spectral features are provided by labels and vertical lines, indicating the presence of a broad Balmer series and the distinctive Mg II $\lambda$2798 absorption line. These characteristics are also commonly observed in other SNe II/IIP, such as SNe 1999em, 2005cs,

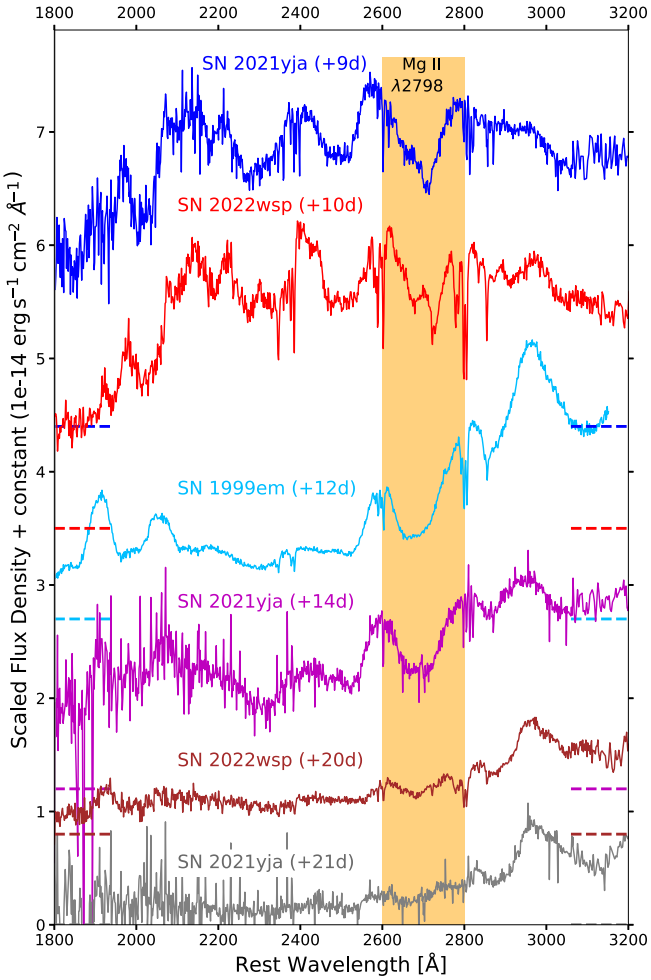


**Figure 2.** Zoomed-in view of the HST/STIS UV spectra of SN 2022wsp at +10 and +20 days for clearer comparison to Type IIP SNe 1999em (Baron et al. 2000) and 2021yja (Vasylyev et al. 2022). All spectra have been dereddened and are in units of $1 \times 10^{-14}$ erg s$^{-1}$ cm$^{-2}$ Å$^{-1}$. The spectra have the same scaling with the exception of SN 1999em, which was scaled by a factor of 0.5. From top to bottom, the flux density spectra have been offset vertically by 4.4, 3.5, 2.7, 1.2, 0.8 ($\times 10^{-14}$ erg s$^{-1}$ cm$^{-2}$ Å$^{-1}$); the zero-points are indicated by horizontal dashed lines.

2005ay, 2012aw, 2013ej, and 2021yja (Baron et al. 2000; Brown et al. 2007; Gal-Yam et al. 2008; Bufano et al. 2009; Bayless et al. 2013; Vasylyev et al. 2022).

The spectrum blueward of ∼3000 Å is dominated by a blend of Fe II, Fe III, and Ni III lines, causing significant line blanketing (Dessart & Hillier 2005). A series of broad emission peaks over this wavelength range can be attributed to regions of reduced line blanketing (Brown et al. 2007). Approximately 43% of the total flux is emitted in the UV (shortward of 3200 Å for both SN 2021yja and SN 2022wsp on days 9 and 10, respectively). Our observations provide further evidence of the general consistency in spectroscopic properties between SN 2022wsp and other SNe II/IIP, supporting the notion that they likely have similar progenitors and explosion mechanisms.

Figure 2 compares the UV spectra of SN 2022yja at +10 and +20 days with those of the Type IIP SNe 1999em (Baron et al. 2000) and 2021yja (Vasylyev et al. 2022). While previous studies have suggested UV homogeneity among SN IIP spectra, our data reveal both similarities and clear differences. These variations could result from a combination of factors, including differences in progenitor radius, explosion-date uncertainty, metallicity, density profile, photospheric temperature, velocity, reddening, and preexplosion behavior.

Figure 1 demonstrates a general agreement between SN 2022wsp and SN 2021yja at wavelengths longer than 3000 Å, around both +10 and +20 days. However, we observe some notable differences in the shape of the UV flux at wavelengths below 3000 Å at ∼10 days, despite comparable observation epochs with tight constraints on the explosion date (<24 hr). Notably, the UV flux continuum of SN 2022wsp appears to be elevated, with more pronounced emission and absorption features, when compared to that of SN 2021yja.

Modeling of the spectroscopic properties of SNe II/IIP during the early photospheric phase using the non–local thermodynamic equilibrium (non-LTE) radiative-transfer code CMFGEN (Hillier 1998) have been carried out in previous studies (see, e.g., SN 1999em; Dessart & Hillier 2005). The modeling addressed that the shape of the UV spectrum is highly sensitive to a set of physical parameters. Specifically, a larger progenitor radius, a steeper radial density profile of the ejecta, a higher photospheric temperature, a lower metallicity, and a lower reddening can each produce a raised UV continuum, without significantly affecting the optical continuum. However, there exists a partial degeneracy between these parameters, particularly between reddening, photospheric temperature, and metallicity. A more detailed discussion of modeling parameters is presented in Section 3.4. Our modeling of the early UV spectra of SN 2022wsp demonstrates a general agreement with that of SN 2021yja, although there may be plausible variations in the explosion properties. The differences in the spectra become less apparent around day +20.

As discussed by Vasylyev et al. (2022), the Mg II λ2798 line is of particular interest in the UV. Its shape has been used by previous studies to infer explosion properties of SNe II, such as the origin of the UV emission (Brown et al. 2007). On day +10, SN 2022wsp exhibits a distinct double-trough feature in the absorption component of Mg II (see the 2600–2800 Å range in Figure 2), which was not seen in any previous observations such as SNe 1999em, 2005cs, 2005ay, 2012aw, 2013ej, and 2021yja (Baron et al. 2000; Brown et al. 2007; Gal-Yam et al. 2008; Bufano et al. 2009; Bayless et al. 2013; Vasylyev et al. 2022). In SN 2021yja, the absence of a double trough in the Mg II absorption region could be a consequence of faster ejecta velocities relative to SN 2022wsp. We test this assumption by performing a Gaussian convolution on the SN 2022wsp spectrum on day +10 (see Figure A1). The convolved SN 2022wsp Mg II profile ($\sigma = 2500$ km s$^{-1}$) shows reasonable agreement with that of SN 2021yja, suggesting that the lack of a double-trough feature can be explained by the latter's higher ejecta velocity (see Section 3.4.1).

As discussed below in Section 3.4, the double-trough Mg II λ2798 profile can be well fitted by the one-dimensional radiative-transfer code, TARDIS. The surprisingly good reproduction suggests that the dip on the blue side is likely the result of overlapping Fe II or Fe III lines formed in a region close to the photosphere, rather than from an external source or developed from a complex geometry that may require further fine-tuning of the model parameters. The shape of this line changes rapidly over a few days, emphasizing the importance of performing observations over short time intervals. In Figure 2, the feature blueward of the Mg II λ2798 absorption can be identified only at day +10 and has

vanished by day +20. Other prominent features seen from SN 2022wsp include the Fe II line at 2900 Å and Ti II line blanketing around 3000 Å as labeled in Figure 1. These lines of singly ionized species were also identified in SNe 2021yja (Vasylyev et al. 2022) and 2005cs (Bufano et al. 2009), and modeled in SN 1999em (Dessart & Hillier 2005).

The day +10 spectrum of SN 2022wsp presents a box-shaped flux excess around 2400 Å, which completely disappeared by day +20. Interestingly, this feature is also evident in the CMFGEN model spectrum discussed by Dessart & Hillier (2005; see their Figure 3) and Dessart & Hillier (2006; see their Figures 10 and 11) for SN 1999em on day +12, despite the observed spectrum displaying a relatively flat bump. It should be noted that this boxy feature resembles the absorption curve of Fe II in the rectified spectra modeled for SN 1999em near 2400 Å (see Figure 3 of Dessart & Hillier 2005). The superposition of Fe II together with Fe III form the trough in the SN 2021yja spectrum (day +9) near 2000 Å, which are also present in the +10 day spectrum of SN 2022wsp.

The spectra presented in Figure 2 are distinct from those of peculiar Type II SNe such as SN 1987A, which display a sharp cutoff in the UV flux below 3000 Å (Kirshner et al. 1987; Pun et al. 1995) by around 10 days after explosion. SN 1987A was the explosion of a blue supergiant (BSG), rather than the red supergiant (RSG) progenitor of typical SNe II/IIP. BSGs are expected to be more compact than RSGs and therefore cool more rapidly, increasing UV flux opacity due to line blanketing by metals at an earlier phase than SN 2022wsp. Additionally, other SNe II that present clear evidence of ejecta-CSM interaction may show UV spectroscopic properties that are distinct from those of normal SNe II/IIP. For example, a significantly blueshifted component in the Mg II $\lambda$2798 P Cygni profile and a rather smooth and elevated continuum below ~2600 Å were reported for the Type IIb SN 2013df (Ben-Ami et al. 2015).

### 3.3. The Optical Spectrum

Optical spectra of SN 2022wsp were obtained at the same phases as our UV observations and are presented in Figure 1. As in the UV, the day +10 spectrum of SN 2022wsp appears to be very similar to the day +9 spectrum of SN 2021yja in the optical. Both SNe can be described by the superposition of a relatively featureless continuum and a series of P Cygni profiles of Balmer lines with blueshifted ($\geqslant$7000 km s$^{-1}$) absorption minima.

There are, however, some subtle but important differences between the early-time spectra of SNe 2022wsp and 2021yja. For example, a suppressed, double-peaked H$\alpha$ profile can be identified in the day +10 spectrum of SN 2022wsp, which then develops into a more typical P Cygni emission shape by day +20. By contrast, the SN 2021yja H$\alpha$ line resembles a more typical, rounded P Cygni profile. In Section 3.4, we show that the fits fail to reproduce the strong suppression and the double-peaked shape, suggesting that interaction may be occurring with a preexisting CSM. One interpretation is that the ejecta interacting with CSM can effectively dampen the strength of the Balmer-line profiles through the "top-lighting" effect (Branch et al. 2000). The suppressed H$\alpha$ line blends together with He I $\lambda$6678, forming a weak double-peaked, asymmetric emission feature. Meanwhile, the He I $\lambda$5876 line is more defined in both epochs of SN 2022wsp compared with SN 2021yja.

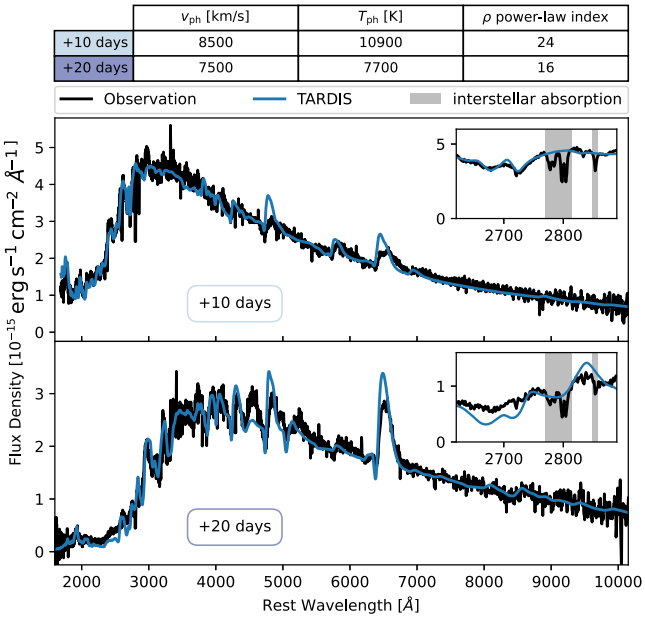


**Figure 3.** TARDIS fits to the HST STIS UV-optical spectra of SN 2022wsp at days +10 (top) and +20 (bottom). The best-fit parameters are presented above the top panel. The embedded subpanels at upper right present a zoomed-in view of the Mg II $\lambda$2798 feature. The gray-shaded areas mark interstellar absorption lines.

### 3.4. TARDIS Modeling of SN 2022wsp

Sophisticated radiative-transfer codes have been utilized to model SNe II/IIP. For example, Baron et al. (2004) employed PHOENIX, while Dessart & Hillier (2006) and Dessart et al. (2008) made use of CMFGEN to perform detailed analyses of the physical properties of the explosion, such as temperature, density, and ionization structure. In order to extract the physical parameters of the explosion of SN 2022wsp from its early spectroscopic evolution, we utilize a modified version of the Monte Carlo radiative-transfer code TARDIS repurposed for analyzing Type II SNe (Vogl et al. 2019); it was originally developed for SNe Ia (Kerzendorf & Sim 2014).

This code treats hydrogen excitation and ionization under non-LTE conditions, which is essential to accurately model the Balmer emission lines. We conduct a comparative analysis of SN 2022wsp and that of SN 2021yja, following the approach discussed in Section 3.5 of Vasylyev et al. (2022). Similarly, we assumed a power-law density profile of the form $\rho = \rho_0(r/r_0)^{-n}$, where $\rho_0$ denotes the density at a characteristic radius $r_0$ and $n$ represents the power-law index of the radial density profile. The calculation also assumes a homogeneous composition. The models vary in the steepness of the density profile $n$, as well as the temperature, velocity, metallicity, and time since explosion.

In addition to the parameters intrinsic to the SN explosion, we fit for different values of the host extinction, $E(B-V)_{\rm host}$. The fitting is carried out using a machine-learning emulator, trained on a large grid of TARDIS simulations as described by Vogl et al. (2020). We use the most up-to-date grid of models as described by Csörnyei et al. (2023; see their Table 2) for the training.

Figure 3 shows our TARDIS fits to the HST UV and optical spectra of SN 2022wsp obtained on days +10 and +20. The plot includes a table containing the key fit parameters, namely the photospheric velocity $v_{\rm ph}$, the photospheric temperature $T_{\rm ph}$

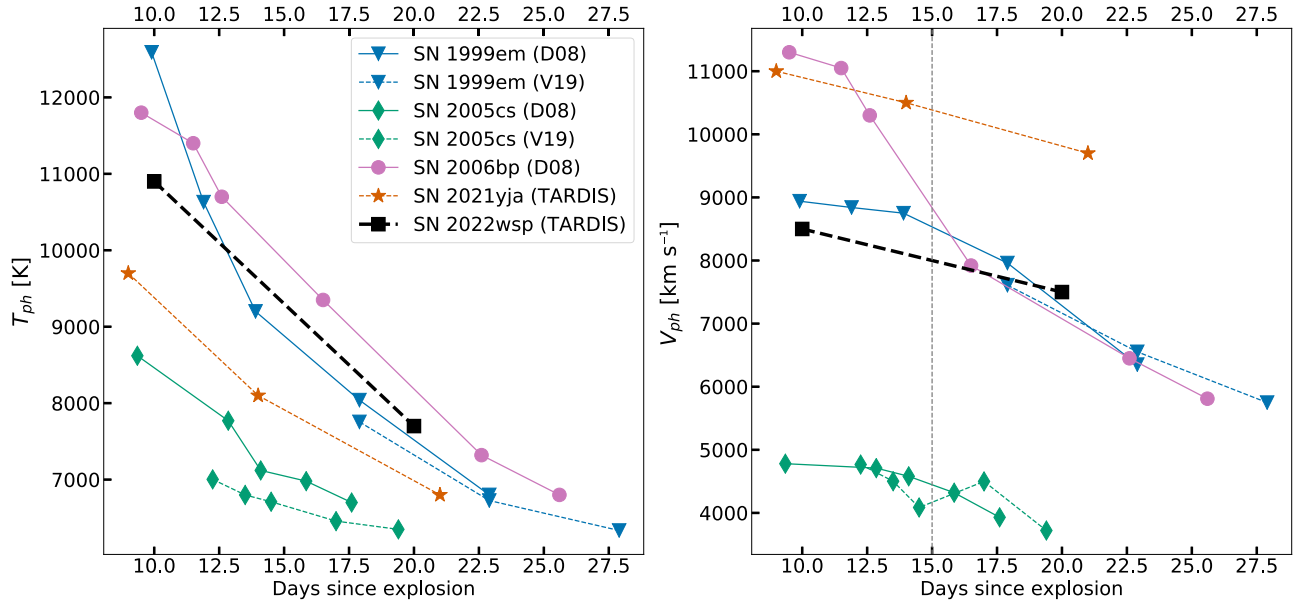


**Figure 4.** Temporal evolution of the photospheric temperature $T_{\rm ph}$ (left) and photospheric velocity $v_{\rm ph}$ (right) of SN 2022wsp obtained from the TARDIS fit to its days +10 ($T_{\rm ph}$=10,900 K, $v_{\rm ph}$ = 8500 km s$^{-1}$) and +20 ($T_{\rm ph}$=7700 K, $v_{\rm ph}$ = 7500 km s$^{-1}$) spectra compared to those of SNe 1999em, 2005cs, 2006bp, and 2021yja (Dessart et al. 2008, D08; Vogl et al. 2019, V19; Vasylyev et al. 2022). Vertical dashed line indicates the velocity at days +15, $v_{\rm d15}$, for comparison purposes.

(i.e., the gas temperature at the photosphere), and $n$. Additional model fits for independently varied parameters are shown in Figures A2–A4 of the Appendix. Similarly to Dessart & Hillier (2006), we argue comparable constraints on photospheric temperature and velocity to within 500 K and 10%, respectively. The best-fit model indicates the presence of significant additional extinction from the host galaxy, with an estimated value of $E(B-V)_{\rm host} \approx 0.3$ mag, as well as a solar metallicity. We note that a supersolar (2 $Z_{\odot}$) metallicity provides a better fit below 1800 Å on day +10 when varied independently and other best-fit parameters are fixed (see Figure A5). Given the uncertainties in the modeling, such as the approximate non-LTE treatment of metal species and the degeneracy between metallicity, temperature, and extinction, we provide only a qualitative estimate for the metallicity. In contrast to SN 2021yja, the emission components of the Balmer P Cygni profiles in the SN 2022wsp spectra, particularly H$\alpha$, are not well fit by TARDIS. Such a discrepancy may be due to Balmer-line suppression by interaction with an ambient H-rich envelope.

An embedded panel in Figure 3 presents a zoomed-in version on the Mg II $\lambda$2798 absorption feature for both epochs. Remarkably, the best-fit TARDIS model reproduces the double-trough profile that was initially discussed in Section 3.2. Such agreement between the observed spectrum and model suggests that the dip centered around 2675 Å is most likely an Fe II transition formed within a part of the ejecta, rather than a high-velocity component from an external source or developed from a complex geometry that may require further fine-tuning of the model parameters. The narrow Mg II $\lambda\lambda$2795, 2802 absorption doublets are excluded in the fitting procedure since they originate from the host galaxy and the Milky Way.

We have chosen to report the inferred parameters as point estimates rather than including their associated uncertainties. Obtaining realistic uncertainties from spectral fits presents substantial challenges. The inherent simplifications within the TARDIS code, such as the power-law density profile and spherical symmetry, as well as certain missing or approximated physical processes, result in discrepancies between the model and observed data. These discrepancies manifest as intricate correlations across the wavelength range, which cannot be adequately addressed by treating them as white noise. As incorporating uncorrelated observational noise would lead to underestimated parameter uncertainties, a more appropriate approach would involve developing a likelihood function that accounts for the complex correlations present in the residuum, as demonstrated by Czekala et al. (2015) for stellar spectra. However, devising such a function falls beyond the scope of this work. Consequently, we present point estimates for the inferred parameters and encourage future research to tackle the challenge of constructing a suitable likelihood function to more accurately determine uncertainties.

#### 3.4.1. Evolution of the Photospheric Temperature and Velocity

In Figure 4, we compare the photospheric temperature and velocity of SN 2022wsp with those of other well-studied SNe II/IIP. The physical parameters presented here are all derived based on modeling of the UV-to-optical spectra. The photospheric temperature of SN 2022wsp at days +10 and +20 is 10,900 and 7700 K, respectively, both falling within the range typically found in SNe IIP at similar phases. At early times ($\sim +12$ days), the photospheric temperatures among these SNe span a wide range (~8500–12,000 K).

The evolution of the temperature of SNe IIP declines roughly linearly with time (at >10 days) until it asymptotically approaches ~6000 K, signaling the onset of the hydrogen recombination phase. The photospheric temperature is similar to that of SNe 1999em and 2006bp, which is on the higher end of the range. SN 2022wsp has a significantly higher inferred photospheric temperature than SNe 2021yja and 2005cs. If all other fitting parameters were held constant for both SNe, the UV flux level is expected to be higher for SN 2022wsp at a similar epoch owing to the higher $T_{\rm ph}$. As shown in Figure 1 and discussed in Section 3.2, the UV flux in the spectrum of

SN 2022wsp is elevated as compared with that of SN 2021yja, consistent with the significantly higher $T_{\rm ph}$ inferred from our modeling.

The photospheric velocity of SN 2022wsp at days +10 and +20 gives 8500 and 7500 km s$^{-1}$, respectively, as inferred from our TARDIS modeling. The velocity scale and evolution of SN 2022wsp also agree with those derived from other SNe II/IIP presented in Figure 4. The velocities of the H$\alpha$ absorption minima are consistent with those obtained from the TARDIS modeling. However, it is worth noting that for SNe IIP, the Fe II absorption minimum (e.g., $\lambda$5169) is the preferred method of estimating the photospheric velocity (Hamuy et al. 2001; Leonard et al. 2002; Dessart & Hillier 2005). For SN 2022wsp, the absorption minimum velocity of the Fe II $\lambda$5169 line is ∼7000 km s$^{-1}$ on day +20, consistent with both the velocities of the H$\alpha$ absorption minimum and TARDIS modeling at that epoch. Moreover, the photospheric velocity at day +15 serves as a reliable indicator of the explosion energy (Dessart et al. 2010). Based on the inferred photospheric velocities of SN 2022wsp, which are comparable to those of SN 1999em at +15 days, it is likely that the two SNe have similar explosion energies.

#### 3.4.2. Radial Density Profile

Early-time observations of SNe II suggest a steep density profile in the outer layers of the ejecta, which gradually flattens over time as the photosphere recedes into the inner layers (Dessart et al. 2008; Vogl et al. 2019). The inferred values of the radial density index $n$ are presented in the rightmost column of Figure 3. In the case of SN 2022wsp, a steep density profile is required to account for the strong suppression of the Balmer lines, especially H$\alpha$ and H$\beta$. The power-law indices obtained from the fits for the first and second epochs are 24 and 16, respectively. The steep density profile suggests that the line-forming region is confined to a region close to the photosphere.

The main effect of lowering the density-profile index is to increase the contrast of the spectral features in the UV and optical (for examples, see Figure 9 of Vogl et al. 2020 and Section 4.5 of Dessart & Hillier 2005). Given the relatively small change in photospheric velocity (∼15%) between days +10 and +20, it is possible to set the same density profile for both epochs using a steeper value than day +20 ($n \approx 20$) and still obtain a reasonable match with the observed spectrum (see behavior of varying $n$ in Figure A4). However, the mismatch in the feature strengths for the first epoch become more severe with this density-index value. It is worth noting that the density profile could have been altered by interaction, so it is uncertain whether a power law provides an appropriate description of the outer layers of the ejecta. The values for $n$ obtained for SN 2022wsp are similar to those inferred from TARDIS modeling of SN 2021yja (Vasylyev et al. 2022).

A significant overlap exists in the line-formation regions between the two epochs, even when considering the very steep density profiles inferred, as the difference in their photospheric velocities is only ∼1000 km s$^{-1}$. Consequently, both epochs probe approximately the same part of the density profile and should in turn favor a similar power-law index. However, this is not the case for SN 2022wsp, indicating a physical scenario that involves ongoing CSM interaction. Furthermore, the TARDIS models fail to reproduce the significant suppression of the Balmer lines in the first epoch. The only feasible way for these models to emulate this suppression is by selecting a very steep density profile, which subsequently results in features that are overly narrow and exhibit extremely blueshifted emission peaks. Dessart et al. (2008) encounter a similar issue using the CMFGEN models for SN 2006bp, which also exhibit line-shape mismatches and potentially unphysical alterations in the density profile between epochs. Ultimately, these discrepancies suggest that there might be a missing element in the models. For SN 2022wsp, this could potentially be interaction in the form of top-lighting or a more intricate density profile.

## 4. Conclusions

We present two epochs of HST/STIS UV-optical spectra on days +10 and +20 of the young, nearby, and relatively highly reddened Type IIP SN 2022wsp. The UV spectrum of SN 2022wsp is compared with that of previously studied SNe having high-S/N data at similar epochs. Although SN 2022wsp fits well within the framework of other well-studied SNe IIP, there are a few key differences in the spectra. The Mg II P Cygni profile displays an unprecedented double-trough feature on day +10 that disappears by day +20. The origin of the blueward dip is most likely an overlapping Fe II line. Overall, the differences in the spectra become less apparent around day ∼20, highlighting the importance of conducting early-time observations in the UV to accurately constrain these parameters. Using the TARDIS code, the observed spectra were best fit by a photospheric velocity of 8500 (7500) km s$^{-1}$, a photospheric temperature of 10,900 (7700) K, a power-law index of 24 (16), and a solar metallicity on day +10 (20). The double-trough feature near the Mg II absorption component is well fitted by this best-fit model. However, the suppressed emission components of H$\alpha$ and H$\beta$ are not represented by the TARDIS fit at day +10, suggesting that the outer layers of the ejecta may be interacting with CSM at these early phases. This is in contrast to SN 2021yja, which did not show evidence of ongoing interaction at similar phases. However, further investigation is needed to determine the validity of this interpretation. A follow-up paper to this work will present a detailed analysis of SN 2022wsp optical spectroscopy, photometry, and spectropolarimetry (Vasylyev et al., 2023, in preparation).

## Acknowledgments

This research was funded by HST grants AR-14259 and GO-16656 from the Space Telescope Science Institute (STScI), which is operated by the Association of Universities for Research in Astronomy (AURA), Inc., under NASA contract NAS5-26555. Additional generous financial support was provided to A.V.F.'s supernova group at U.C. Berkeley by Gary and Cynthia Bengier, Alan Eustace, Sunil Nagaraj, Steven Nelson, Landon Noll, Sandy Otellini, Christopher R. Redlich, Sanford Robertson, Clark and Sharon Winslow, Briggs and Kathleen Wood, and many other donors. C.V. was supported for part of this work by the Excellence Cluster ORIGINS, which is funded by the Deutsche Forschungsgemeinschaft (DFG, German Research Foundation) under Germany's Excellence Strategy-EXC-2094-390783311. G. S's research was supported through the Cal NERDS and UC LEADS programs. M.M. acknowledges support in part from ADAP program grant 80NSSC22K0486, NSF grant AST-2206657, and HST program GO-16656.

This research made use of TARDIS, a community-developed software package for spectral synthesis of SNe (Kerzendorf & Sim 2014; Kerzendorf et al. 2022). The development of TARDIS received support from GitHub, the Google Summer

of Code initiative, and ESA's Summer of Code in Space program. TARDIS is a fiscally sponsored project of NumFOCUS. TARDIS makes extensive use of Astropy and Pyne.

*Software:* Astropy (Astropy Collaboration et al. 2013, 2018), TARDIS (Kerzendorf & Sim 2014; Vogl et al. 2019), uvotpy (Kuin 2014), DAOPHOT (Stetson 1987), IDL Astronomy user's library (Landsman 1993), SOUSA pipeline (Brown et al. 2014), Pyne (Scopatz et al. 2012).

## Appendix

A comparison of the Gaussian-convolved SN 2022wsp spectrum with that of SN 2021yja is presented in Figure A1. TARDIS fits to the HST STIS UV-optical spectra of SN 2022wsp at days +10 (top) and +20 (bottom) for independently varied parameters ($T_{\rm ph}$, $v_{\rm ph}$, $n$, and $Z$) are shown in Figures A2–A5.

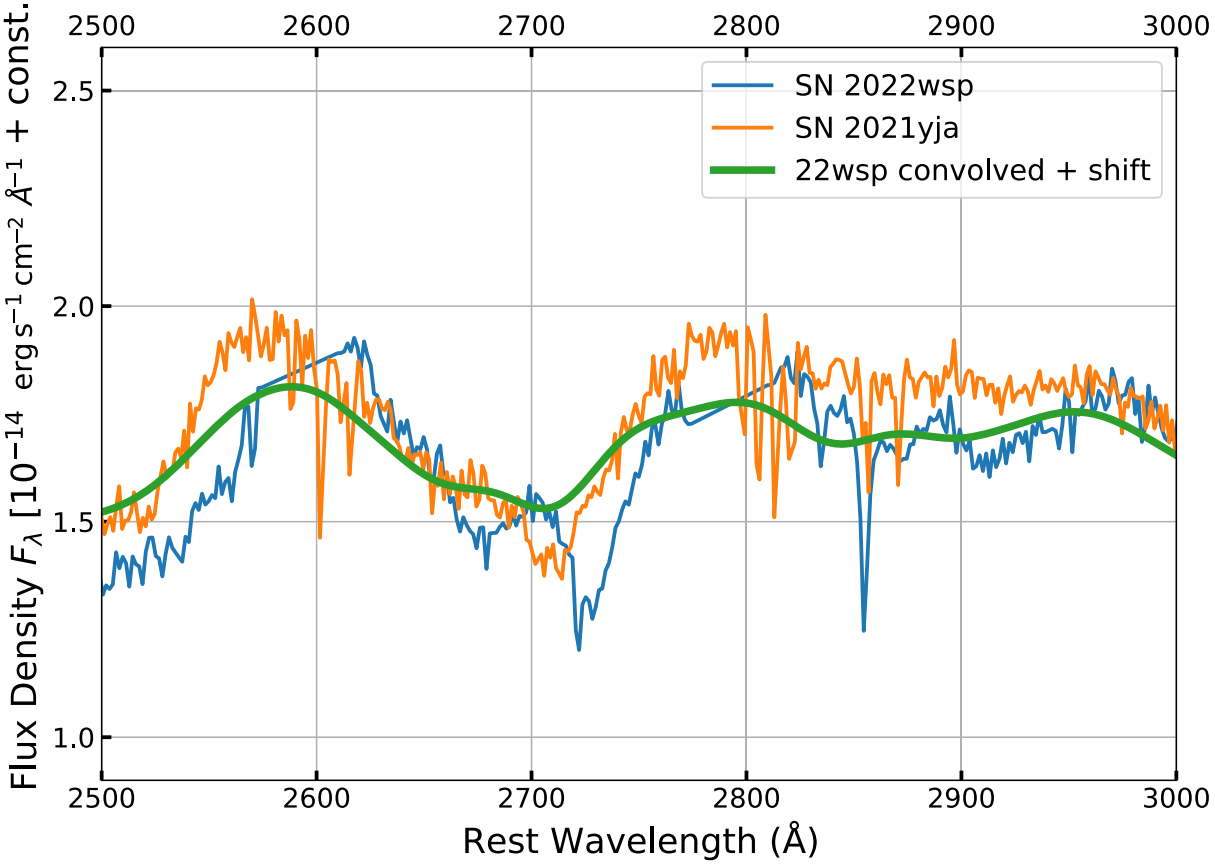


**Figure A1.** Gaussian-convolved spectrum of SN 2022wsp ($\sigma = 2500$ km s$^{-1}$; green) compared to observed SN 2021yja (blue) and SN 2022wsp (orange) spectra. Wavelength range is zoomed in on the Mg II profile. The convolved spectrum is blueshifted by 1250 km s$^{-1}$ to match the spectral features with SN 2021yja. All spectra are dereddened.

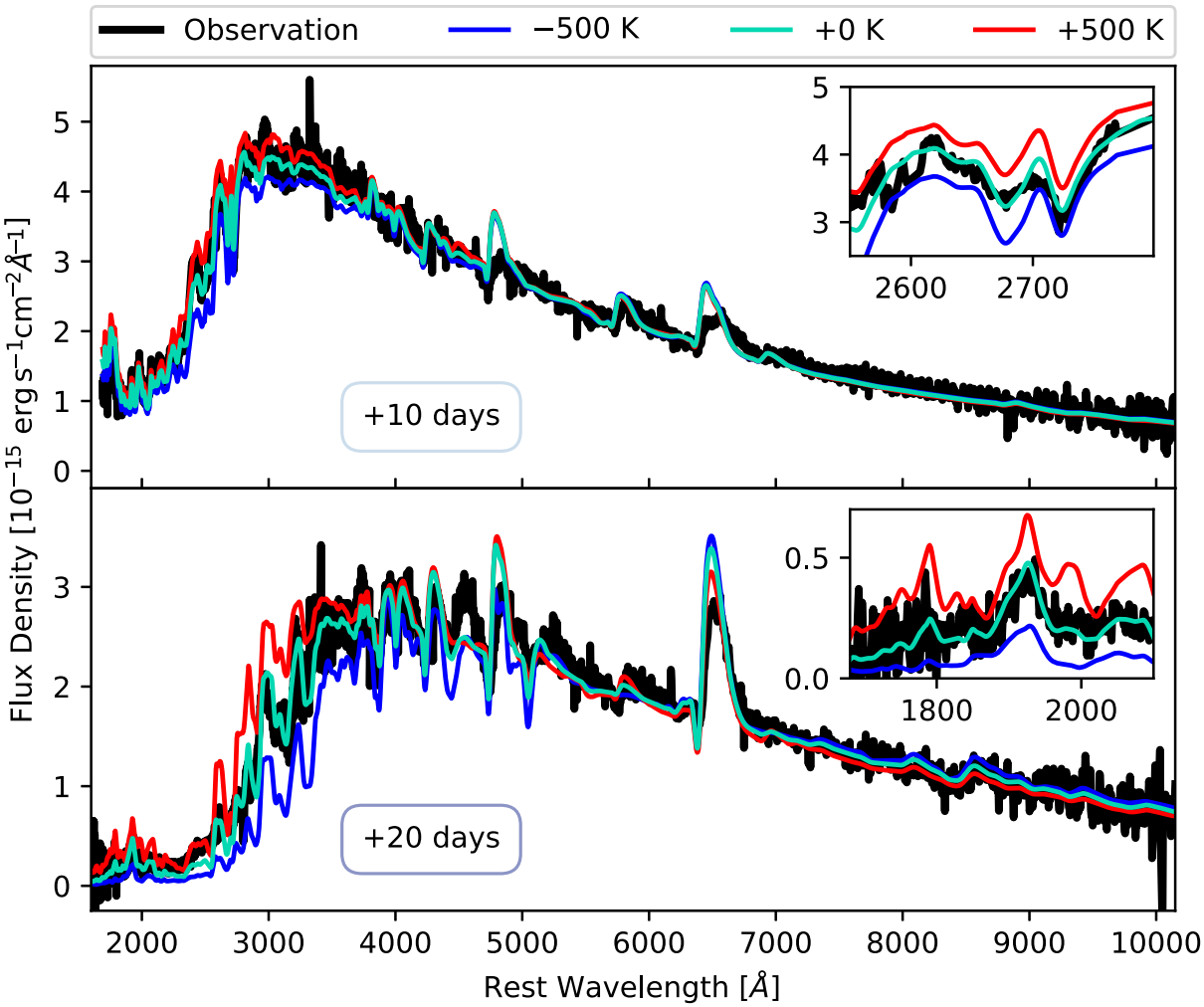


**Figure A2.** TARDIS fits to the HST STIS UV-optical spectra of SN 2022wsp at days +10 (top) and +20 (bottom) for varied $T_{\rm ph}$ (all other parameters fixed). The two temperature deviations from the best-fit value (turquoise) on day +10 ($T_{\rm ph,best}$ = 10,900 K) and day +20 ($T_{\rm ph,best}$=7700 K) are represented as $T_{\rm ph,best}$ − 500 K (blue) and $T_{\rm ph,best}$ + 500 K (red). The black curve represents observational data. Insets provide a detailed view of specific wavelength regions for easier comparison.

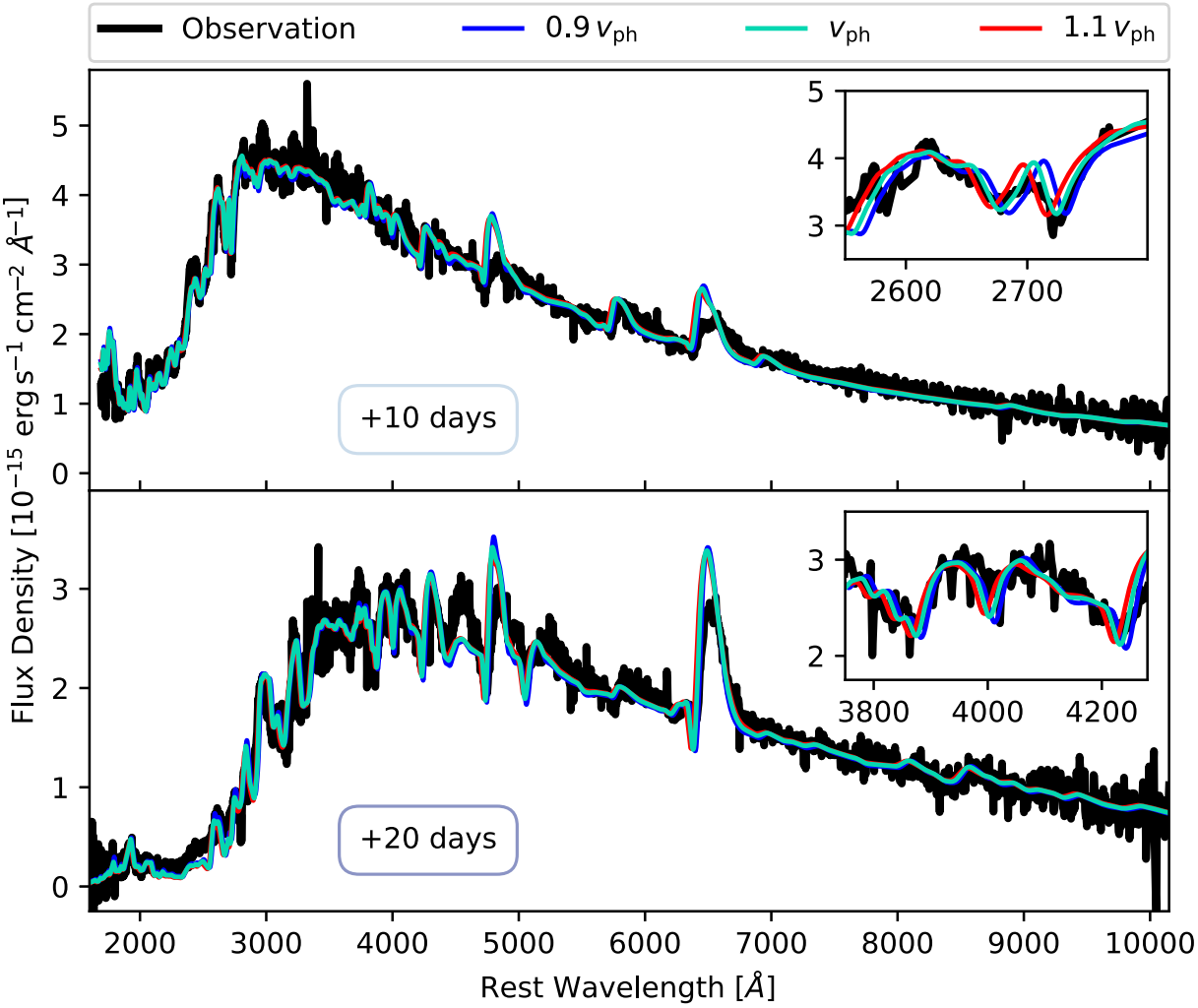


**Figure A3.** Same as Figure A2 but instead varying the photospheric velocity relative to the best-fit model $v_{\rm ph,best} = 8500(7500)$ km s$^{-1}$ at day +10 (20). The two photospheric velocity variations are $0.9v_{\rm ph,best}$ (blue) and $1.1v_{\rm ph,best}$ (red).

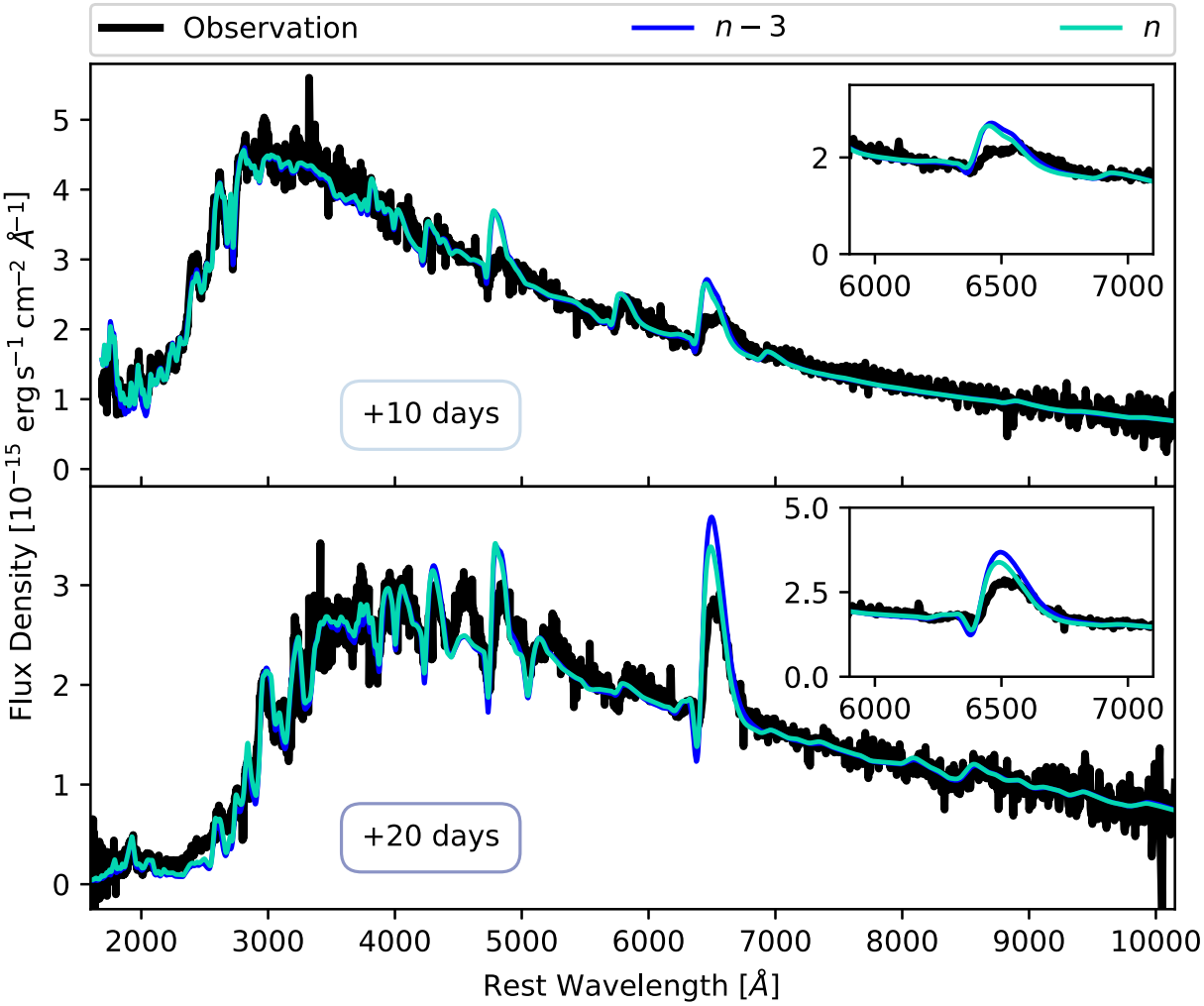


**Figure A4.** Same as Figure A2 but instead varying the density-profile index $n$ relative to the best-fit model $n_{\rm best} = 24(16)$ on days $+10(20)$. Density-profile variations are $n_{\rm best} - 3$ (blue) and $n_{\rm best}$ (turquoise).

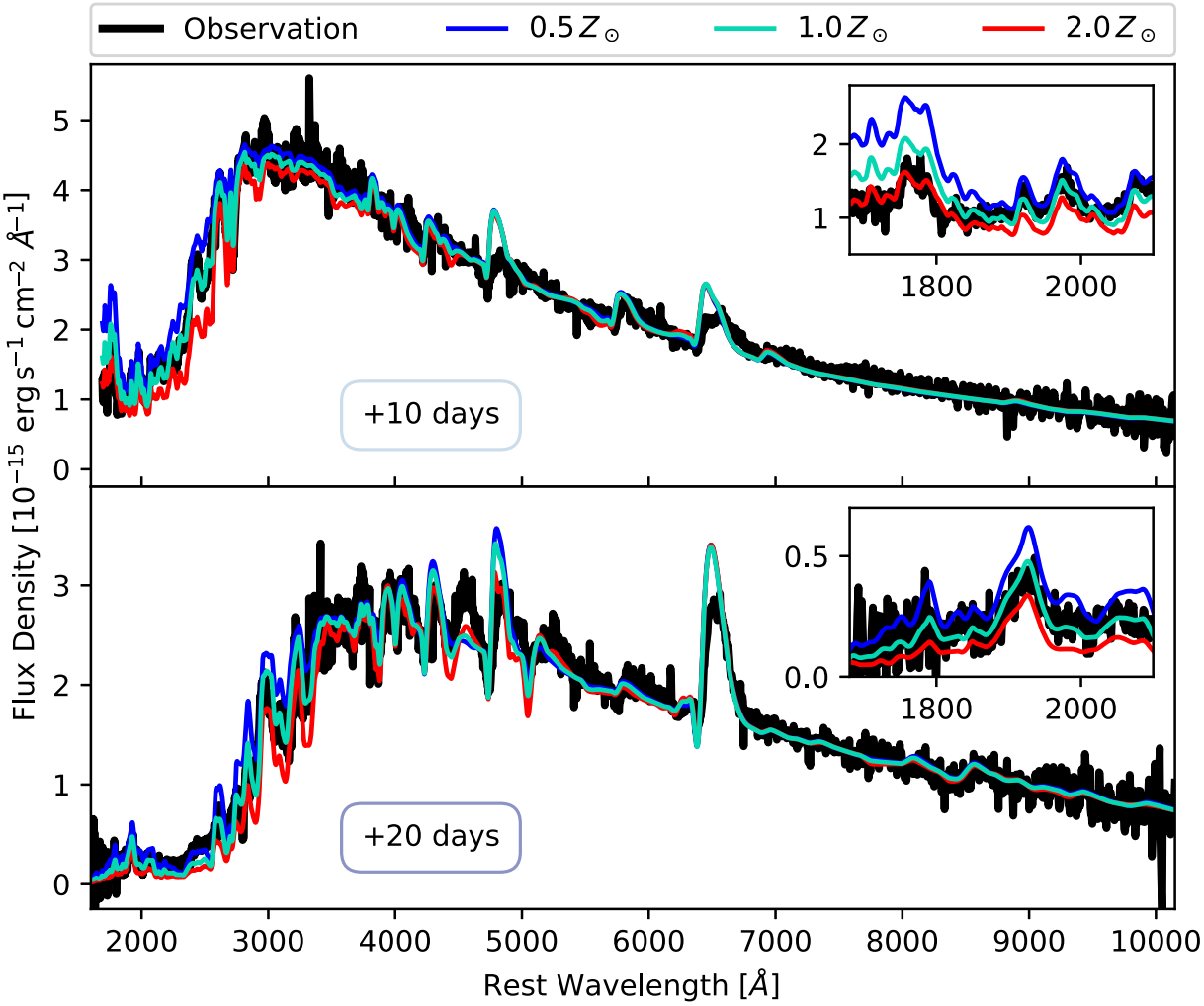


**Figure A5.** Same as Figure A2 but instead varying the metallicity $Z$ for values 0.5 $Z_\odot$ (blue), 1.0 $Z_\odot$ (turquoise), and 2.0 $Z_\odot$ (red).

## ORCID iDs

Sergiy S. Vasylyev https://orcid.org/0000-0002-4951-8762
Christian Vogl https://orcid.org/0000-0002-7941-5692
Yi Yang (杨轶) https://orcid.org/0000-0002-6535-8500
Alexei V. Filippenko https://orcid.org/0000-0003-3460-0103
Thomas G. Brink https://orcid.org/0000-0001-5955-2502
Peter J. Brown https://orcid.org/0000-0001-6272-5507
Thomas Matheson https://orcid.org/0000-0001-6685-0479
Maryam Modjaz https://orcid.org/0000-0001-7132-0333
Avishay Gal-Yam https://orcid.org/0000-0002-3653-5598
Paolo A. Mazzali https://orcid.org/0000-0001-6876-8284
Thomas de Jaeger https://orcid.org/0000-0001-6069-1139
Kishore C. Patra https://orcid.org/0000-0002-1092-6806
Gabrielle E. Stewart https://orcid.org/0009-0000-2503-140X

## References

Anderson, J. P., González-Gaitán, S., Hamuy, M., et al. 2014, ApJ, 786, 67
Astropy Collaboration, Price-Whelan, A. M., Sipőcz, B. M., et al. 2018, AJ, 156, 123
Astropy Collaboration, Robitaille, T. P., Tollerud, E. J., et al. 2013, A&A, 558, A33
Baron, E., Branch, D., Hauschildt, P. H., et al. 2000, ApJ, 545, 444
Baron, E., Nugent, P. E., Branch, D., & Hauschildt, P. H. 2004, ApJL, 616, L91
Bayless, A. J., Pritchard, T. A., Roming, P. W. A., et al. 2013, ApJL, 764, L13
Ben-Ami, S., Hachinger, S., Gal-Yam, A., et al. 2015, ApJ, 803, 40
Bostroem, K. A., Valenti, S., Sand, D. J., et al. 2022, TNSTR, 2022-2882, 1
Branch, D., Jeffery, D. J., Blaylock, M., & Hatano, K. 2000, PASP, 112, 217
Brown, P. J., Breeveld, A. A., Holland, S., Kuin, P., & Pritchard, T. 2014, Ap&SS, 354, 89
Brown, P. J., Dessart, L., Holland, S. T., et al. 2007, ApJ, 659, 1488
Bufano, F., Immler, S., Turatto, M., et al. 2009, ApJ, 700, 1456
Cardelli, J. A., Clayton, G. C., & Mathis, J. S. 1989, ApJ, 345, 245
Csörnyei, G., Vogl, C., Taubenberger, S., et al. 2023, A&A, 672, A129
Czekala, I., Andrews, S. M., Mandel, K. S., Hogg, D. W., & Green, G. M. 2015, ApJ, 812, 128
Dessart, L., Blondin, S., Brown, P. J., et al. 2008, ApJ, 675, 644
Dessart, L., & Hillier, D. J. 2005, A&A, 437, 667
Dessart, L., & Hillier, D. J. 2006, A&A, 447, 691
Dessart, L., Livne, E., & Waldman, R. 2010, MNRAS, 408, 827
Dhungana, G., Kehoe, R., Vinko, J., et al. 2016, ApJ, 822, 6
Filippenko, A. V. 1997, ARA&A, 35, 309
Gal-Yam, A. 2017, in Handbook of Supernovae, ed. A. W. Alsabti & P. Murdin (Cham: Springer International Publishing), 195
Gal-Yam, A., Bufano, F., Barlow, T. A., et al. 2008, ApJL, 685, L117
Hamuy, M., Pinto, P. A., Maza, J., et al. 2001, ApJ, 558, 615
Hillier, D. J. 1998, ApJ, 496, 407
Kerzendorf, W., Sim, S., Vogl, C., et al. 2022, tardis-sn/tardis: TARDIS v2022.2.27, vrelease-2022.2.27, Zenodo, 10.5281/zenodo.6299948
Kerzendorf, W. E., & Sim, S. A. 2014, MNRAS, 440, 387
Kirshner, R. P., Sonneborn, G., Crenshaw, D. M., & Nassiopoulos, G. E. 1987, ApJ, 320, 602

Kuin, P., 2014 UVOTPY: Swift UVOT grism data reduction, Astrophysics Source Code Library, ascl:1410.004
Landsman, W. B. 1993, in ASP Conf. Ser. 52, Astronomical Data Analysis Software and Systems II, ed. R. J. Hanisch et al. (San Francisco, CA: ASP), 246
Leonard, D. C., Filippenko, A. V., Gates, E. L., et al. 2002, PASP, 114, 35
Lu, N. Y., Hoffman, G. L., Groff, T., Roos, T., & Lamphier, C. 1993, ApJS, 88, 383
Mazzali, P. A. 2000, A&A, 363, 705
Modjaz, M., Gutiérrez, C. P., & Arcavi, I. 2019, NatAs, 3, 717
Nagao, T., Pastorello, A., & Reguitti, A. 2022, TNSCR, 2022-2910, 1
Prichard, L., Welty, D., & Jones, A. 2022, (Baltimore: STScI)
Pun, C. S. J., Kirshner, R. P., Sonneborn, G., et al. 1995, ApJS, 99, 223
Riess, A. G., Yuan, W., Macri, L. M., et al. 2022, ApJL, 934, L7
Rubin, A., & Gal-Yam, A. 2016, ApJ, 828, 111
Sanders, N. E., Soderberg, A. M., Gezari, S., et al. 2015, ApJ, 799, 208
Schlafly, E. F., & Finkbeiner, D. P. 2011, ApJ, 737, 103
Scopatz, A. M., Romano, P. K., Wilson, P. P., & Huff, K. D. 2012, TrANS, 107, 985
Stetson, P. B. 1987, PASP, 99, 191
Tartaglia, L., Sand, D. J., Valenti, S., et al. 2018, ApJ, 853, 62
Valenti, S., Howell, D. A., Stritzinger, M. D., et al. 2016, MNRAS, 459, 3939
Vasylyev, S. S., Filippenko, A. V., Vogl, C., et al. 2022, ApJ, 934, 134
Vogl, C., Kerzendorf, W. E., Sim, S. A., et al. 2020, A&A, 633, A88
Vogl, C., Sim, S. A., Noebauer, U. M., Kerzendorf, W. E., & Hillebrandt, W. 2019, A&A, 621, A29
Williamson, M., Vogl, C., Modjaz, M., et al. 2023, ApJL, 944, L49